 CMES, vol.15, no.1, pp.1-16, 2006

Meshless Local Petrov-Galerkin (MLPG) Mixed Finite Difference Method for Solid Mechanics

S. N. Atluri[1], H. T. Liu[2], and Z. D. Han[2]

Abstract: The Finite Difference Method (FDM), within the framework of the Meshless Local Petrov-Galerkin (MLPG) approach, is proposed in this paper for solving solid mechanics problems. A "mixed" interpolation scheme is adopted in the present implementation: the displacements, displacement gradients, and stresses are interpolated independently using identical MLS shape functions. The system of algebraic equations for the problem is obtained by enforcing the momentum balance laws at the nodal points. The divergence of the stress tensor is established through the generalized finite difference method, using the scattered nodal values and a truncated Taylor expansion. The traction boundary conditions are imposed in the stress equations directly, using a local coordinate system. Numerical examples show that the proposed MLPG mixed finite difference method is both accurate and efficient, and stable.

keyword: Meshless method, Finite difference method, MLPG

1 Introduction

The meshless method, as indicted by its name, is a computational method, which does not require a mesh discretization of the domain of the problem. As compared to its mesh-based counterpart, viz., the finite element method, the meshless method has its inherent advantages, due to the elimination of elements and therefore, element-related limitations, such as the element-dependent phenomena in crack propagation, the inability in dealing with severe element distortions, and the cost of producing high-quality meshes for complex structures. The meshless method has been accepted by researchers and engineers as a successful alternative to the finite element method for some classes of problems, such as the crack propagation problems. Tremendous efforts have been put into the research and practice of the meshless approaches, such as the smooth particle hydrodynamics (SPH) and the element free Galerkin method (EFG). However, these approaches require certain meshes or background cells for the purpose of integration of the weak form, and therefore are not truly meshless methods. Recently, Atluri and Zhu [Atluri and Zhu (1998); Atluri (2004)] proposed the Meshless Local Petrov-Galerkin (MLPG) approach, in which both the trial functions and the test functions are constructed on local subdomains, and no background integration cells are required. Therefore, the MLPG method is a truly meshless method for solving the general problems defined by Partial Differential Equations (PDEs). A general review and discussion on the meshless method in general, and the MLPG approach in particular, can be found in the monograph by Atluri (2004).

The MLPG method provides the flexibility in the choice of the test and trial functions, and therefore makes it possible to construct various meshless implementations, by combining different trial and test functions. For example, in Han and Atluri (2004), a series of MLPG approaches is constructed for solving elasto-static problems. They adopted the Moving Least Squares (MLS) as well as the augmented Radial Basis Functions (RBF) as the trial functions; and the Heaviside function, Dirac delta function and the Kelvin fundamental elasticity solutions were alternatively adopted as the test functions.

Generally speaking, the meshless method is intrinsically more expensive than the traditional element-based method such as the finite element method, due to the fact that the meshless interpolation usually involves more nodes and has more complex shape functions. This complexity, and the attendant high computational expense, prevent the meshless method from fully fulfilling its potential. In a series of efforts to simplify and speed up the meshless implementation, Atluri et al. (2004) proposed the so-called MLPG "mixed" finite volume method, in which both the displacements and the displacement-

[1] Center for Aerospace Research & Education, University of California, Irvine, CA
[2] Knowledge Systems Research, LLC, GA

gradients are interpolated using the identical shape functions, independently. As a result, the continuity requirement on the trial functions is reduced by one order, and the complex second derivatives of the shape function are avoided. In addition, the Heaviside function is adopted as the test function and the domain integration in the local weak form is eliminated. High-performance implementations of the MLPG mixed finite volume method (MFVM) were reported for elastostatic problems [Atluri, Han, Rajendran (2004), Han, Atluri (2004a)], elasto-dynamic problems [Han, Atluri (2004b)], nonlinear problems [Han, Rajendran, Atluri (2005)], and dynamic problems with large deformation and rotation [Han et al. (2006); Liu et al. (2006a)].

In an effort to further improve the efficiency of the MLPG implementation, Atluri et al. (2006b) proposed a MLPG "mixed" collocation method, in which the Dirac delta function is adopted as the test function, and therefore the system of equations is established at nodal points only. In the collocation implementation, the traction boundary conditions are imposed by a penalty method, and the displacement boundary conditions are applied directly to the system of equations by the standard collocation approach. The MLPG mixed collocation method has achieved a great success, since it results in a stable convergence rate, while being much more efficient than the MLPG finite volume method.

In this paper, we explore the implementation of the MLPG finite difference method for solid mechanics problems. The idea of using the finite difference method in approximating the derivatives of a function, and in solving elasticity problems, can be traced to the early work of Jensen (1972) and Perrone and Kao (1975). In their implementation, the truncated Taylor series was adopted to form the finite difference operator on arbitrary grids. Liszka and co-workers (1996) developed a new version of the finite difference method, called hp-Meshless cloud method, using the MLS to fit the truncated Taylor series on a set of nodal values. In their implementations, the finite difference equations were constructed directly from the neighboring nodal values and therefore a strong node- distribution dependence was observed. In addition, the system of equations at the traction-boundary nodes was established directly from the boundary equations; and these were not compatible with the in-domain nodal equations formed by the linear force balance law. In the present MLPG mixed finite difference method, we define a *shrink factor,* and the sampling points are shifted from the nodal points. The system of equations is constructed by using the same linear force balance law for both the in-domain as well as the boundary nodes, and thus the incompatibility is removed. To increase the stability, and reduce the smoothness requirement on the shape functions, the "mixed" interpolation scheme is adopted: the displacements, displacement gradients, and stresses are interpolated independently using identical MLS shape functions. The traction boundary conditions are imposed on the stress equations directly.

2 Formulations

In this section, we formulate an MLPG mixed finite difference method for solving linear solid mechanics problems.

2.1 Meshless Interpolation

Among the available meshless approximation schemes, the moving least squares (MLS) is generally considered to be one of the best methods to interpolate random data with a reasonable accuracy, because of its completeness, robustness and continuity. The MLS is adopted in the current MLPG finite difference method; while the implementation of other meshless interpolation schemes is straightforward within the present framework. For completeness, the MLS approximation is briefly reviewed here, and a more detailed discussion on the MLS can be found in Atluri (2004).

With the MLS interpolation, a function $u(\mathbf{x})$ can be approximated over a number of scattered local points (nodes) $\{\mathbf{x}_I\}$, $(I = 1,2,...,m)$ as

$$u(\mathbf{x}) = \mathbf{p}^T(\mathbf{x})\mathbf{a}(\mathbf{x}) \tag{1}$$

where $\mathbf{p}^T(\mathbf{x})$ is a monomial basis, and $\mathbf{a}(\mathbf{x})$ is an undetermined-coefficient vector. The linear monomial basis can be expressed as $\mathbf{p}^T(\mathbf{x}) = [1, x_1, x_2]$ for two-dimensional problems and $\mathbf{p}^T(\mathbf{x}) = [1, x_1, x_2, x_3]$ for three dimensional problems, respectively. The coefficient-vector $\mathbf{a}(\mathbf{x})$ is determined by minimizing the weighted discrete L_2 norm, defined as

$$J(\mathbf{x}) = \sum_{I=1}^{m} w_I(\mathbf{x})[\mathbf{p}^T(\mathbf{x}_I)\mathbf{a}(\mathbf{x}) - \widehat{u}^I]^2 \tag{2}$$

where $w_I(\mathbf{x})$ are the weight functions and $\widehat{u}^I$ are the fictitious nodal values, respectively. A fourth order spline weight function is used in the present study. Once the coefficient vector $\mathbf{a}(\mathbf{x})$ is determined and substituted into Eq. (1), the function $u(\mathbf{x})$ can be approximated by these nodal values as

$$u(\mathbf{x}) = \sum_{J=1}^{m} \Psi^J(\mathbf{x})\hat{u}^J \tag{3}$$

where $\hat{u}^J$ is the virtual nodal value at node J, and $\Psi^J(\mathbf{x})$ is the shape function. It is well known that the MLS shape function does not have the Dirac Delta property. However, the trial functions can be expressed in term of the true nodal values with the use of mapping relationship between the virtual and true nodal values, as [Atluri, Kim and Cho (1999)]

$$u(\mathbf{x}) = \sum_{J=1}^{m} \Phi^J(\mathbf{x})u^J \tag{4}$$

2.2 Mixed Approach

For a linear elastic body Ω undergoing infinitesimal deformations, the equations of balance of linear and angular momentum can be written as

$$\sigma_{ij,j} + f_i = 0; \quad \sigma_{ij} = \sigma_{ji}; \quad ()_{,i} \equiv \frac{\partial}{\partial x_i} \tag{5}$$

Here and in the following parts of the paper, the tensor notation is adopted, and a repeated index implies summation. The boundary conditions are given as

$$\begin{aligned} &u_i = \overline{u}_i \text{ on } \Gamma_u \\ &t_i = \sigma_{ij}n_j = \overline{t}_i \text{ on } \Gamma_t \end{aligned} \tag{6}$$

In the above equations, f_i is the body force; $\overline{u}_i$ and $\overline{t}_i$ are the prescribed displacements and tractions on the displacement boundary Γ_u and the traction boundary Γ_t, respectively. n_i is the outward unit normal to the boundary Γ. In the present study, the isotropic linear elastic constitutive relation is assumed, namely the stress tensor σ_{ij} is linearly related to the strain tensor ε_{ij} as

$$\sigma_{ij} = C_{ijkl}\varepsilon_{kl} = C_{ijkl}[\frac{1}{2}(u_{i,j} + u_{j,i})] \tag{7}$$

where C_{ijkl} is the elasticity tensor, which has the property of $C_{ijkl} = C_{jikl}$.

In the traditional implementation, the meshless approximation in Eq. (4) can be used to interpolate the displacements in Eq. (7). Thereafter, the stresses and strains are determined from a direct-differentiation of the displacements in the whole solution domain. Such differentiation operations are required in forming the system equations whenever the derivatives are involved in integrals. It has been well accepted in most element-based methods, in which the simple shape functions are defined based on the element shape. However, this implementation is not efficient in the meshless methods, because i) the meshless approximation is not efficient in calculating such derivatives everywhere in the domain, especially when the MLS approximation is used; ii) the requirement of the completeness and continuity of the shape functions is one-order higher for smoother derivatives.

In the present study, the mixed approach is used for the derivatives [Atluri (2004)]. First, Eq. (4) can be used to interpolate displacements, as the shape function is used for the nodal displacement variables in the traditional implementation, as

$$u_i(\mathbf{x}) = \sum_{K=1}^{m} \Phi^K(\mathbf{x})u_i^K \tag{8}$$

In addition, the same shape function is also used for the displacement gradients, as

$$u_{i,j}(\mathbf{x}) = \sum_{K=1}^{m} \Phi^K(\mathbf{x})u_{i,j}^K \tag{9}$$

or for the stresses

$$\sigma_{ij}(\mathbf{x}) = \sum_{K=1}^{m} \Phi^K(\mathbf{x})\sigma_{ij}^K \tag{10}$$

where u_i^K, $u_{i,j}^K$ and σ_{ij}^K are the nodal values of displacements, displacement gradients and stresses at the point $\mathbf{x}^K$, respectively, which can be treated as an independent set of variables. Without losing generality, by differentiating the displacements in Eq. (8) with respect to x_j *at each nodal point* $\mathbf{x}^K$, we obtain:

$$u_{i,j}^K \equiv \frac{\partial u_i}{\partial x_j}(\mathbf{x}^K) = \sum_{J=1}^{n} \frac{\partial \Phi^J(\mathbf{x}^K)}{\partial x_j} u_i^{(J)} \equiv \sum_{J=1}^{n} R_j^{KJ} u_i^J \tag{11}$$

Thus, Eq. (9) can be written as:

$$u_{i,j}(\mathbf{x}) = \sum_{K=1}^{m}\sum_{J=1}^{n} \Phi^K(\mathbf{x})R_j^{KJ}u_i^J \tag{12}$$

Like wise, we may define from Eqs. (7), (10), and (11):

$$\sigma_{ij}(\mathbf{x}) = \sum_{K=1}^{m} \sum_{J=1}^{n} C_{ijkl} \Phi^K(\mathbf{x}) R_l^{KJ} u_k^J \tag{13}$$

where, by definition, the transformation matrix $\mathbf{R}$ is constant and banded, and can be applied to the strains and stresses. Thus, the nodal displacement gradient variables as well as stresses are expressed in terms of the nodal displacement variables. The number of system equations is then kept as the same number as the nodal-displacement variables, after the transformation. In addition, such a transformation is performed locally, and the system matrix retains its bandedness. For numerical implementation, it is not necessary to calculate and store the matrix R explicitly.

With the use of the mixed approach, the derivatives of the displacements as well as other secondary field variables keep the same order of the completeness and smoothness as the primary variable. Only lower-order polynomial terms are required in the meshless approximations, and a smaller nodal influence size can be chosen, to speed up the calculation of the shape functions. Any additional differentiation operations are avoided when performing the integrals to form the system equations. It improves the efficiency of the meshless methods dramatically, which is demonstrated by solving same typical examples.

In summary, the mixed MLPG method allows for a simple way to relate the displacement-gradients as well as the stresses to the nodal displacements, without differentiate displacement field everywhere.

2.3 Finite Difference Operator

Now, we present an alternate approach, based on generalized finite-difference method, for determining the gradients of the displacements at arbitrarily distributed nodes in a meshless approximation, from the values of the displacement at these same nodes.

From the MLS interpolation, for a node I,there exit several neighbor-nodes which influence the values of an interpolated variables at node I, as shown in Figure 1. For a neighbor node J, $\mathbf{h}^{JI} = \mathbf{x}^J - \mathbf{x}^I$, represents the distance-vector between nodes J and I. A *shrink factor* $\varsigma(0 < \varsigma \leq 1)$ is defined here, to locate a sampling point between the node J and I (the squares in Figure 1). We expand the displacement vector in the vicinity of node I,

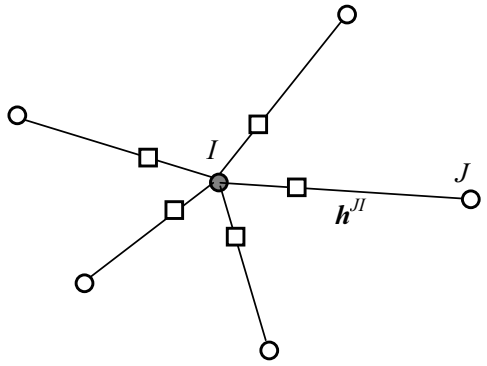

Figure 1 : The finite difference scheme: the circles represent the neighbor nodes of I and the squares denote the sampling points for the finite difference scheme.

as:

$$u_i(\mathbf{x}) = u_i^I + \left(x_j - x_j^I\right) u_{i,j}^I + O\left(\left|\mathbf{x} - \mathbf{x}^I\right|^2\right) \tag{14}$$

Here, $u_i^I = u_i^{(}\mathbf{x}^I)$ and $u_{i,j}^I = u_{i,j}^{(}\mathbf{x}^I)$ are the nodal values of the displacements, and their gradients at node I, respectively. Therefore, the error between the linear Taylor expansion, and the displacement-gradient at the sampling points J, can be expressed as

$$err^J = u_i^I + \varsigma h_j^{JI} u_{i,j}^I - u_i(\mathbf{x}^I + \varsigma \mathbf{h}^{JI}) \tag{15}$$

By considering all the sampling points around node I, the weighted discrete L_2 error norm is defined as:

$$L(\mathbf{x}) = \sum_{J=1}^{m} w_J(\mathbf{x}) \left[u_i^I + \varsigma h_j^{JI} u_{i,j}^I - u_i(\mathbf{x}^I + \varsigma \mathbf{h}^{JI})\right]^2 \tag{16}$$

Here, $w_J(\mathbf{x})$ are the weight functions, which are chosen to be the same as the weight functions in the MLS. By minimizing the weighted discrete L_2 norm in Eq. (16), the displacement gradients at node I can be calculated as:

$$\begin{aligned} u_{i,j}^I &= \sum_{J=1}^{m} H_{jJ} \left[u_i(\mathbf{x}^I + \varsigma \mathbf{h}^{JI}) - u_i^I\right] \\ &\equiv \sum_{J=1}^{m} H_j^J u_i(\mathbf{x}^I + \varsigma \mathbf{h}^{JI}) - \overline{H}_j u_i^I \end{aligned} \tag{17}$$

Here, $\overline{H}_j = \sum_{J=1}^{m} H_j^J$ and $\mathbf{H} = \left(\mathbf{A}^T\mathbf{W}\mathbf{A}\right)^{-1}\mathbf{A}^T\mathbf{W}$ with

$$\mathbf{A} = \varsigma \begin{bmatrix} \mathbf{h}^{1I} \\ \vdots \\ \mathbf{h}^{mI} \end{bmatrix} \text{ and } \mathbf{W} = \begin{bmatrix} w_1 & 0 & 0 \\ 0 & \ddots & 0 \\ 0 & 0 & w_m \end{bmatrix} \tag{18}$$

It should be mentioned that the dimension of matrix $\mathbf{A}$ is decided by the number of the neighbor nodes of node I. Based on the requirement of MLS, we have more independent neighbor nodes for a linear or higher order monomial basis. Therefore, the system represented in Eq. (17) is usually an overdetermined system and thus the inverse of the matrix $\mathbf{A}$ exists.

With the meshless interpolation for the displacements, we evaluate $u_i(\mathbf{x}^I + \varsigma\mathbf{h}^{JI})$ from Eq. (8) as:

$$u_i(\mathbf{x}^I + \varsigma\mathbf{h}^{JI}) = \sum_{K=1}^{n} \Phi^K(\mathbf{x}^I + \varsigma\mathbf{h}^{JI})u_i^K \tag{19}$$

Thus the displacement gradients at node I in Eq. (17) can be expressed as

$$\begin{aligned} u_{i,j}^I &= \sum_{J=1}^{m}\sum_{K=1}^{n} H_j^J \Phi^K(\mathbf{x}^I + \varsigma\mathbf{h}^{JI})u_i^K - \overline{H}_j u_i^I \\ &\equiv \sum_{J=1}^{M} \Theta_j^J u_i^J - \overline{H}_j u_i^I \end{aligned} \tag{20}$$

in which, some more neighbor nodes may be introduced because $u_i(\mathbf{x}^I + \varsigma\mathbf{h}^{JI})$ in Eq. (17) may have different neighbor nodes other than those of the node I. The coefficient matrixes Θ_j^J and $\overline{H}_j$ are constant and banded locally. Thus the direct differentiation operation $\Phi_{,j}^J(\mathbf{x}^K)$ in Eq. (11) can be replaced by the operator developed in Eq. (20), through the meshless interpolation.

It should be pointed out that the differential operator defined in Eq. (20) is very general, and not limited to the differentiation of the displacements. In conjunction with the mixed approach, this operation can be used to calculate any higher-order independent variables, instead of differentiating the shape functions directly. From the numerical point of view, such constant matrixes speed up the efficiency of the algorithm when more differential operations are involved in the PDEs, such as the Nervier-Stokes Equations for the fluid mechanics. Thereafter, the present differential operator be applied for any order of differential operations for higher-order PDEs, in conjunction with the present mixed approach, in a very straight-forward manner.

3 MLPG Methods Based on FD Operator

3.1 MLPG Mixed Finite Difference Method

It is well-known that the MLPG approach is a general framework to formulate various meshless methods for solving various partial differential equations (PDEs). It employs the various test functions within the various local sub-domains. The advantages of the MLPG approach include the lack of any restriction on the choices of the test functions and the local sub-domains. Thereafter, various MLPG methods have been developed and applied to solve different physical problems. A complete summary has been presented in Atluri (2004). In the present study, a general finite difference method is employed to evaluate the divergence of the stress tensor.

With the independent mixed interpolation for the stresses, we can express the derivatives of the stress tensor at node I in Eq. (17) using the neighboring nodal values as

$$\sigma_{ij,k}^I = \sum_{J=1}^{M} \Theta_k^J \sigma_{ij}^J - \overline{H}_k \sigma_{ij}^I \tag{21}$$

The constant coefficient matrixes Θ_j^J and $\overline{H}_j$ are the same as those developed for the displacement gradients in Eq. (20). To establish the system of equations for the elasticity problem, we may enforce the balance of linear momentum at each node, by evaluating the divergence of the stress tensor. This can be expressed as

$$\begin{aligned} \sigma_{ij,j}^I + f_i^I &= \left[\sum_{J=1}^{M} \Theta_j^J \sigma_{ij}^J - \overline{H}_j \sigma_{ij}^I\right] + f_i^I = 0; \\ &\text{for } I = 1,2,...,N \end{aligned} \tag{22}$$

where N is the number of total nodes in the solution domain. The above equation can be rewritten in the matrix form as

$$\mathbf{K}_s^I \cdot \mathbf{S} - \overline{\mathbf{H}}^I \cdot \mathbf{S}^I = \mathbf{f}_b^I; \quad \text{for } I = 1,2,...,N \tag{23}$$

Here, $\mathbf{f}_b^I$ is the body force vector at node I; $\mathbf{S}$ is the nodal stress component vector and $\mathbf{S}^I$ is the stress component vector of node I.

With the constitutive relationship in Eq. (7) and the transformation matrix in Eq. (11) or Eq. (20), we can rewrite the system equations for the nodal displacements as

$$\mathbf{K} \cdot \mathbf{u} = \mathbf{f} \tag{24}$$

With the present finite difference method, the PDEs can be solved locally without explicit local sub-domains. It has been simplified by sharing the same information about the neighbor nodes that was used for the meshless interpolation. This method also completely avoids any direct differentiation of the shape functions. It gives more freedom in choosing the proper meshless interpolation methods.

3.2 Boundary Conditions

For the node on the traction boundary, the stress components should satisfy the traction boundary conditions as

$$\sigma_{ij}^K n_j^K = \overline{t}_i^K; \quad \text{for } K = 1,2,...,N_s \tag{25}$$

with N_s is the number of the traction boundary nodes, and $\mathbf{n}^K$ is the outward normal at the boundary node K. The above equation can be rewritten in term of the stress component vector, as

$$\mathbf{M}^K \cdot \mathbf{S}^K = \overline{\mathbf{t}}^K; \quad \text{for } K = 1,2,...,N_s \tag{26}$$

where $\mathbf{M}^K$ is the general coupling matrix between the stress components, representing the traction boundary conditions.

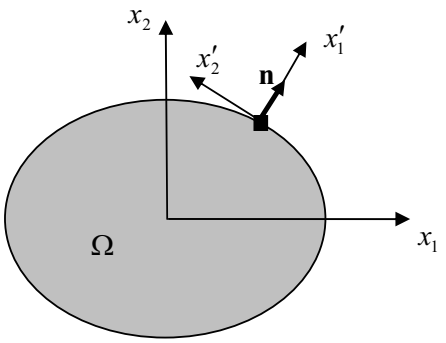

Figure 2 : The local coordinates system.

If the normal $\mathbf{n}^K$ is parallel to the global coordinates, $\mathbf{M}^K$ is a diagonal unit matrix. For the nodes with the normal not being parallel to the global coordinates, a local coordinate system can be defined, by taking the local $\mathbf{x}_1'^K$ direction coinciding with the outward normal direction $\mathbf{n}^K$, as shown in Figure 2. Eq. (26) can be rewritten in the local coordinate system as

$$\mathbf{M}'^K \cdot \mathbf{S}'^K = \overline{\mathbf{t}}^K; \quad \text{for } K = 1,2,...,N_s \tag{27}$$

where

$\mathbf{S}'^K = \mathbf{Q}^K \cdot \mathbf{S}^K$; $\mathbf{M}'^K = \mathbf{M}^K \cdot (\mathbf{Q}^K)^{-1}$and $\mathbf{Q}^K$ is the local transformation matrix between the local and global coordinates. With the use of the local coordinate system, the general coupling matrix $\mathbf{M}'^K$ becomes diagonal and therefore, the stress components, in terms of $\mathbf{S}'^K$, can be solved from the boundary conditions in Eq. (27). Here, we can represent the known stress degrees of freedom (DOFs) at node K as $\mathbf{S}_1'^K = \overline{\mathbf{t}}^K$ and the other unknown stress DOFs as $\mathbf{S}_2'^K$.

With the coordinate transformation, the second term of the system equation in Eq. (22) established on the traction boundary node K can be expressed as

$$\begin{aligned}
\overline{\mathbf{H}}^K \cdot \mathbf{S}^K &= \overline{\mathbf{H}}^K \cdot (\mathbf{Q}^K)^{-1} \cdot \mathbf{S}'^K \\
&= \overline{\mathbf{H}}^K \cdot [(\mathbf{Q}^K)_1^{-1} \cdot \mathbf{S}_1'^K + (\mathbf{Q}^K)_2^{-1} \cdot \mathbf{S}_2'^K] \\
&= \overline{\mathbf{H}}^K \cdot (\mathbf{Q}^K)_1^{-1} \cdot \overline{\mathbf{t}}^K + \overline{\mathbf{H}}^K \cdot (\mathbf{Q}^K)_2^{-1} \cdot \cdot \mathbf{Q}_2^K \cdot \mathbf{S}^K \\
&\equiv \mathbf{f}_s^K + \overline{\mathbf{H}}'^K \cdot \mathbf{S}^K
\end{aligned} \tag{28}$$

where $\mathbf{Q}_1^K$, $\mathbf{Q}_2^K$ and $(\mathbf{Q}^K)_1^{-1}$, $(\mathbf{Q}^K)_2^{-1}$ are the sub-matrixes of $\mathbf{Q}^K$ and its inverse $(\mathbf{Q}^K)^{-1}$ corresponding to the stress DOFs of $\mathbf{S}_1'^K$ and $\mathbf{S}_2'^K$, respectively.

Substituting Eq. (28) back to the system equation in Eq. (22), we have

$$\mathbf{K}_s^K \cdot \mathbf{S} - \overline{\mathbf{H}}'^K \cdot \mathbf{S}^K = \mathbf{f}_b^K + \mathbf{f}_s^K \tag{29}$$

in which the traction boundary conditions have been imposed. It can be also transformed to the displacement-based system equations, as in Eq. (24). Therefore, it is solvable with properly proposed displacement boundary conditions [Han and Atluri (2004a)].

3.3 Comparison between the MLPG Mixed Methods

There are three MLPG mixed methods developed under the MLPG approach: i) MLPG Mixed Finite Volume Method; ii) MLPG Mixed Collocation Method, and iii) MLPG Mixed Finite Difference Method. They all use the mixed approach to interpolate the variables of different orders independently, through the MLS approximation. The mixed approach requires only a first-order polynomial basis in the MLS approximations of both strains as well as displacements. A smaller support size can be used in the present MLPG mixed method, and the number of nodes is reduced dramatically, especially for 3D cases. The local integrals in the present method contain

Table 1 : Comparison between the MLPG mixed methods

A: Meshless interpolation of the displacements		
MLS Approximation	$u_i(\mathbf{x}) = \sum_{K=1}^{m} \Phi^K(\mathbf{x}) u_i^K \ , \ \forall \mathbf{x} \in \Omega ; \qquad u_i^K \equiv u_i(\mathbf{x}^K)$	A1
B: Determine the displacement-gradients and stresses		
Primal Approach (direct differentiation)	$u_{i,j}(\mathbf{x}) = \sum_{K=1}^{m} \Phi^K{}_{,j}(\mathbf{x}) u_i^K \ , \ \forall \mathbf{x} \in \Omega$	B1
	$\sigma_{ij}(\mathbf{x}) = \sum_{K=1}^{m} C_{ijpq} \Phi^K{}_{,q}(\mathbf{x}) u_p^K \ , \ \forall \mathbf{x} \in \Omega$	B2
	$\sigma_{ij,k}(\mathbf{x}) = \sum_{K=1}^{m} C_{ijpq} \Phi^K{}_{,q}(\mathbf{x}) u_p^K \ , \ \forall \mathbf{x} \in \Omega$	B3
Mixed Approach (All derivatives are interpolated independently)	$u_{i,j}(\mathbf{x}) = \sum_{K=1}^{m} \Phi^K(\mathbf{x}) u_{i,j}^K \ , \ \forall \mathbf{x} \in \Omega$ where $u_{i,j}^K \equiv u_{i,j}(\mathbf{x}^K) = \dfrac{\partial u_i}{\partial x_j}(\mathbf{x}^K)$, at the nodal point $\mathbf{x}^K$	B4
	$\sigma_{ij}(\mathbf{x}) = \sum_{K=1}^{m} \Phi^K(\mathbf{x}) \sigma_{ij}^K \ , \ \forall \mathbf{x} \in \Omega$ where $\sigma_{ij}^K \equiv \sigma_{ij}(\mathbf{x}^K) = C_{ijpq} u_{p,q}^K(\mathbf{x}^K)$, at the nodal point $\mathbf{x}^K$	B5
	$\sigma_{ij,k}(\mathbf{x}) = \sum_{K=1}^{m} \Phi^K(\mathbf{x}) \sigma_{ij,k}^K \ , \ \forall \mathbf{x} \in \Omega$ where $\sigma_{ij,k}^K \equiv \sigma_{ij,k}(\mathbf{x}^K) = \dfrac{\partial \sigma_{ij}}{\partial x_k}(\mathbf{x}^K)$, at the nodal point $\mathbf{x}^K$	B6
Combination of Primal & Mixed Approaches	$\sigma_{ij,k}(\mathbf{x}) = \sum_{K=1}^{m} \Phi^K{}_{,k}(\mathbf{x}) \sigma_{ij}^K \ , \ \forall \mathbf{x} \in \Omega$ where σ_{ij}^K is defined in Eq. B5	B7
C: Evaluate the nodal derivative values at the nodal points for the mixed approach		
Direct differentiation	$u_{i,j}^K = \sum_{J=1}^{n} \dfrac{\partial \Phi^J(\mathbf{x}^K)}{\partial x_j} u_i^J \equiv \sum_{J=1}^{n} R_j^{KJ} u_i^J$, at the nodal point $\mathbf{x}^K$	C1
	$\sigma_{ij}^K = \sum_{J=1}^{n} C_{ijpq} R_q^{KJ} u_p^J$, at the nodal point $\mathbf{x}^K$	C2

	$\sigma_{ij,k}^K = \sum_{J=1}^{n} \frac{\partial \Phi^J(\mathbf{x}^K)}{\partial x_k} \sigma_{ij}^J = \sum_{J=1}^{n} R_k^{KJ} \sigma_{ij}^J$, at the nodal point $\mathbf{x}^K$	C3
Finite-difference operator	$u_{i,j}^K = \sum_{J=1}^{M} \Theta_j^K u_i^J - \overline{H}_j u_i^K$, at the nodal point $\mathbf{x}^K$	C4
	$\sigma_{ij}^K = C_{ijpq} (\sum_{J=1}^{M} \Theta_q^K u_p^J - \overline{H}_q u_p^K)$, at the nodal point $\mathbf{x}^K$	C5
	$\sigma_{ij,k}^K = \sum_{J=1}^{M} \Theta_k^K \sigma_{ij}^J - \overline{H}_k \sigma_{ij}^K$, at the nodal point $\mathbf{x}^K$	C6
D: MLPG approach for satisfying equilibrium equations		
Local weak Form	$\int_{\Omega_s} (\sigma_{ij,j} + f_i) v_i d\Omega = 0$, un-symmetric local weak-form where v_i is the test function, Ω_s is the local sub-domain.	D1
	$\int_{\partial\Omega_s} t_i v_i d\Gamma - \int_{\Omega_s} (\sigma_{ij} v_{i,j} - f_i v_i) d\Omega = 0$, symmetric local weak-form	D2
E: Various MLPG methods		
MLPG Mixed Finite Volume Method	Heaviside test function ($v_i = 1$); symmetric local weak-form (Eq. D2); Mixed approach for the stresses (Eq. B5) Direct differentiation of the displacements for the stresses (Eq. C2)	E1
MLPG Mixed Collocation Method	Dirac delta test function ($v_i = \delta(\mathbf{x} - \mathbf{x}^K)$); un-symmetric local weak-form (Eq. D1); Mixed approach for the stresses (Eq. B5) Direct differentiation of the displacements for the stresses (Eq. C2) Direct differentiation of the stresses for their divergence (Eq. C3)	E2
MLPG Mixed Finite Difference Method	Dirac delta test function ($v_i = \delta(\mathbf{x} - \mathbf{x}^K)$); un-symmetric local weak-form (Eq. D1); Mixed approach for the stresses (Eq. B5) Direct differentiation of the displacements for the stresses (Eq. C2) Finite-difference operator of the stresses for their divergence (Eq. C6)	E3

only the strains, without involving the derivatives of the displacement explicitly. Thus, all the mixed methods are more suitable for non-linear problems with large deformations, due to their simplicity and efficiency. However, three methods are different from each other in several aspects, including the local sub-domains, local weak-forms, trial and test functions, and differential operators. They demonstrate the flexibility of the MLPG approach, as a general framework, in developing various meshless methods. A brief summary is presented in Table 1 and a flowchart in Fig. 3.

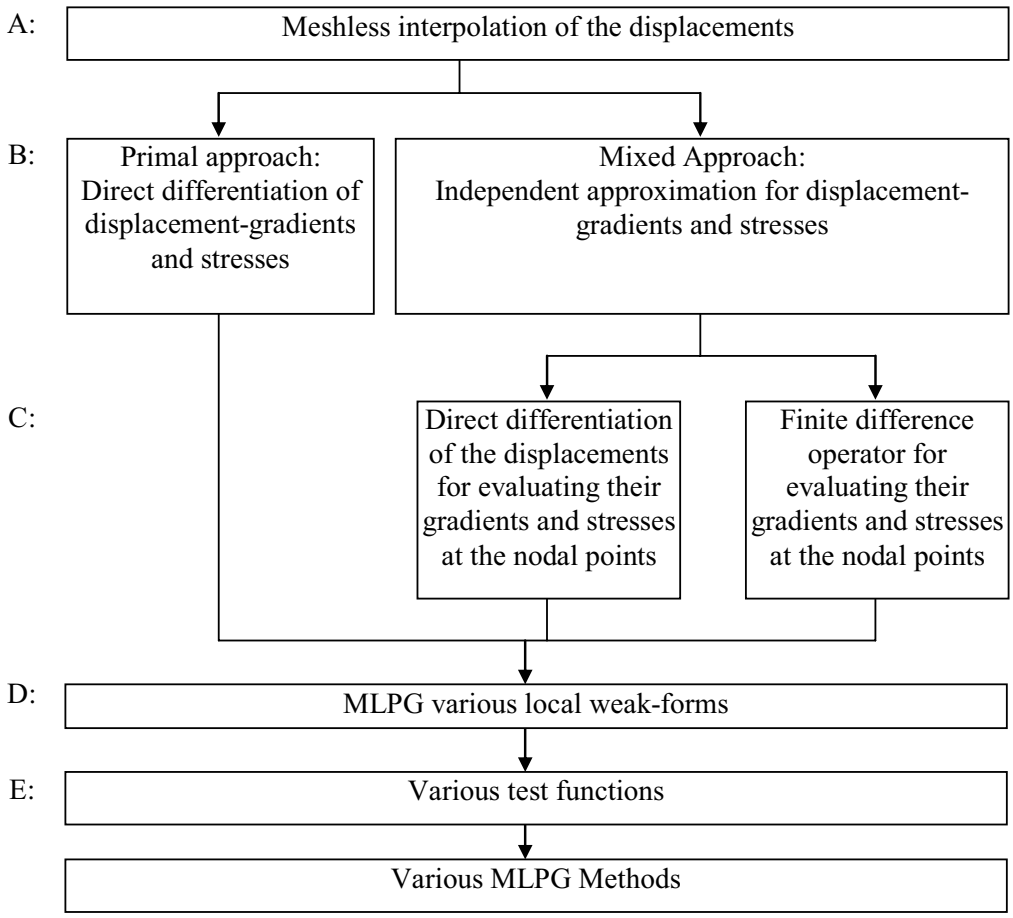

Figure 3 : Flowchart for developing various MLPG methods

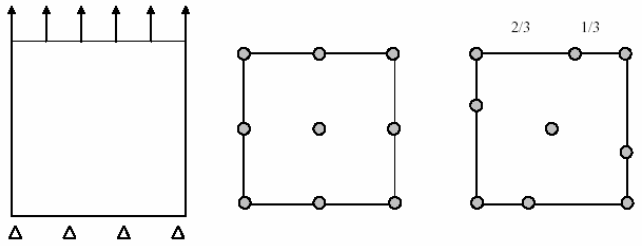

Figure 4 : The patch test: a rectangle under uniform tension. The two nodal configurations

4.1 The Patch Test

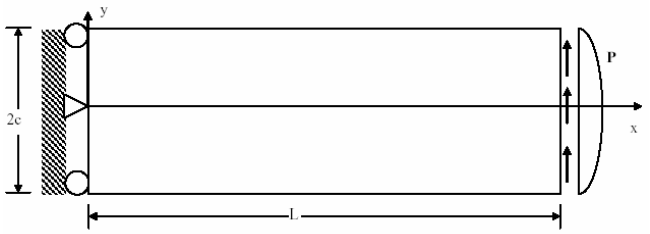

Figure 5 : A cantilever beam under a transverse load at the end

4 Numerical Examples

In this section, several 2D numerical examples, as solved by the proposed meshless finite difference method, are presented. The examples include: 1) the patch test, 2) cantilever beam under transverse loading, 3) curved beam bent by a force at the end, and 4) infinite plate with a circular hole under uniaxial load.

The standard patch test: a rectangular plate under uniform tension load (see Fig. 4) is solved as the first example. The material parameters are as follows: the Young's modulus $E = 1.0$, and the Poisson's ratio $\nu = 0.25$. Plane stress condition is assumed for the 2D problem and 9 nodes are used. Two nodal configurations are used for the

patch: one is regular and another is irregular, as shown in Fig. 4. The proper displacement constraints are applied to the bottom edge.

The simulation results show a linear displacement along the lateral edges, and constant displacement along the top edge; the normal stress in the loading direction is constant and there is no shear stress in the solution domain.

4.2 Cantilever Beam

In the second example, we solve a cantilever beam under a transverse load at the tip, as shown in Fig. 5. For this problem, the exact displacement solution for plane stress is given in Timoshenko and Goodier (1970) as

$$u_x = -\frac{Py}{6EI}\left[3x(2L-x)+(2+\nu)\left(y^2-c^2\right)\right]$$
$$u_y = \frac{Py}{6EI}\left[x^2(3L-x)+3\nu(L-x)y^2+(4+5\nu)c^2x\right] \tag{30}$$

where the moment of inertia $I = c^3/3$.

The problem is solved using the meshless finite difference method under a plane stress condition, with the following constants: $P = 1$, $E = 1$, $c = 2$, $L = 24$, and $\nu = 0.25$. Regular uniform nodal configurations with nodal distances, d, of 2.0, 1.0, 0.5, and 0.33 are used. The corresponding numbers of nodes are 39, 125, 441, and 949, respectively. The nodal configuration for $d = 1.0$ is shown in Fig. 6.

This problem is simulated using the MLS, with a first order monomial basis. The support size is chosen as $1.15d$ and the shrink factor $\varsigma = 0.3$. Fig. 6 shows the normalized vertical displacement at the center of the beam for the nodal configuration with $d = 1.0$. The simulation prediction agrees with the analytical solution very well.

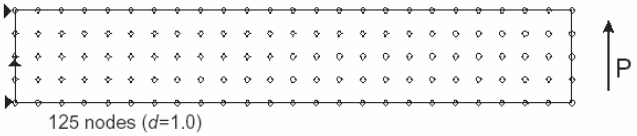

Figure 6 : The nodal configuration of the cantilever beam for d=1.0

The shrink factor ς plays an important role in the finite difference scheme. When $\varsigma = 1.0$, the derivatives of stress are obtained by the finite difference method directly from the neighbor nodal values; while a small

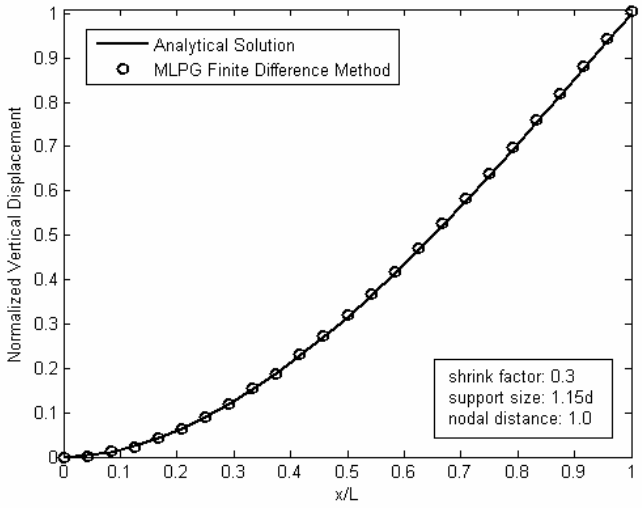

Figure 7 : The normalized vertical displacement of the cantilever beam under the end load

shrink factor confines the finite difference to a close region around the point of interest. In the current study, five shrink factors, ς =0.1, 0.2, 0.3, 0.5, and 1.0 are used to investigate the shrink factor's effect. The relative vertical displacement error defined as follows, is used to represent the accuracy of the simulation in the following parts for this example.

$$\varepsilon = \sqrt{\frac{1}{n}\sum_{i=1}^{n}\left(\frac{\overline{v}_i - v_i}{v_i}\right)^2} \tag{31}$$

Here, v_i and $\overline{v}_i$ are the analytical and calculated vertical displacement component along the center line of the beam, respectively, and n is the total number of nodes involved. The relative displacement errors for the various shrink factors are shown for two nodal configurations (d =1.0 and 0.5) in Fig. 8, and it is seen that a moderate shrink factor leads to better results.

The support size (the size of the influence domain) is another important parameter in meshless approaches. It is related to both the accuracy of the solution, as well as the computational efficiency. On one hand, too small a support size will cause the meshless approximation algorithms singular, since not enough neighbor nodes are included. On the other hand, too large a support size leads to the loss of interpolation locality. In the current study, circular support domains are adopted for the 2D problems, with the radius being defined as the support size. Four support sizes are chosen for the cantilever beam

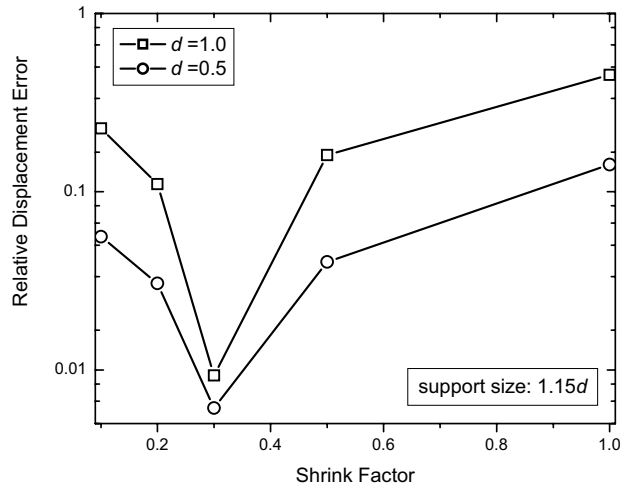

Figure 8 : The influence of the shrink factor in the cantilever beam under the end load

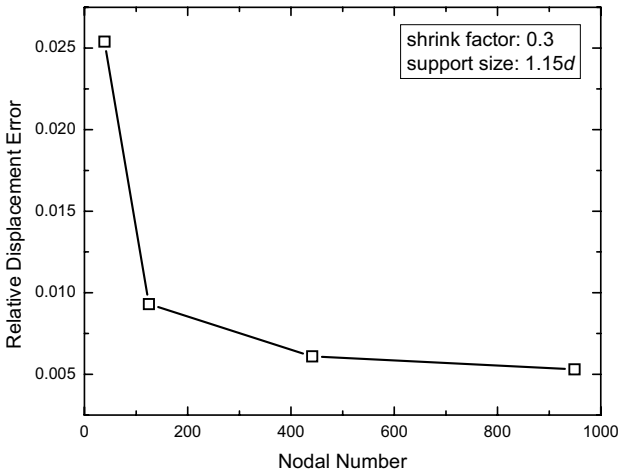

Figure 10 : The convergence rate in the cantilever beam under the end load

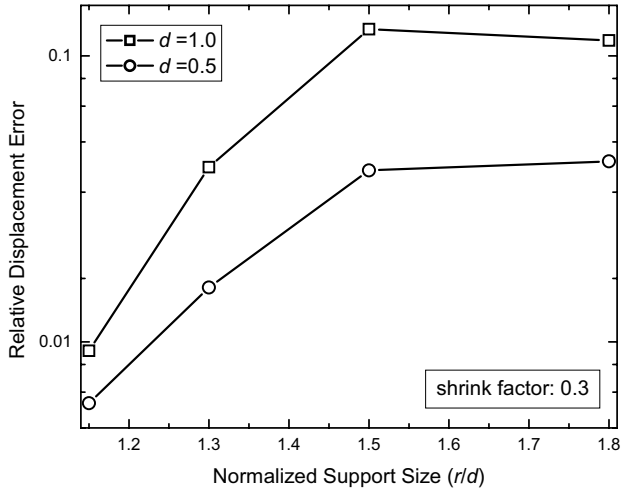

Figure 9 : The influence of the support size in the cantilever beam under the end load

problem, and they are defined to be proportional to the nodal distance, as 1.15, 1.3, 1.5, and 1.8, respectively. Two nodal configurations are used (d =1.0 and 0.5) and the shrink factor is chosen as 0.3 for the current simulations. Fig. 9 shows that accurate results are obtained for small support sizes. This observation is encouraging, since a smaller support size makes the present method even more efficient, by speeding up the MLS approximation and reducing the bandwidth of the stiffness matrix.

The convergence rate is studied with four nodal configurations (d =2.0, 1.0, 0.5, and 0.33). The shrink factor is chosen as 0.3 and the support size is $1.15d$. The relative displacement errors of the vertical displacement are used for showing the convergence rate in Fig. 10. The results clearly show that a stable convergence is obtained for the present meshless finite difference method.

4.3 Curved Beam

In this example, the problem of a curved beam under an end load is used to evaluate the present method. The problem is shown in Fig. 11, for which the following exact displacement solution for plane stress is given in Timoshenko and Goodier (1970):

$$u_r = \frac{P}{E}\left[\sin\theta\left(D(1-\nu)\log r + A(1-3\nu)r^2 + \frac{B(1+\nu)}{r^2}\right) - 2D\theta\cos\theta + K\sin\theta + L\cos\theta\right]$$

$$u_\theta = \frac{P}{E}\left[-\cos\theta\left(-D(1-\nu)\log r + A(5+\nu)r^2 + \frac{B(1+\nu)}{r^2}\right) + 2D\theta\sin\theta + K\cos\theta + L\sin\theta\right] \quad (32)$$

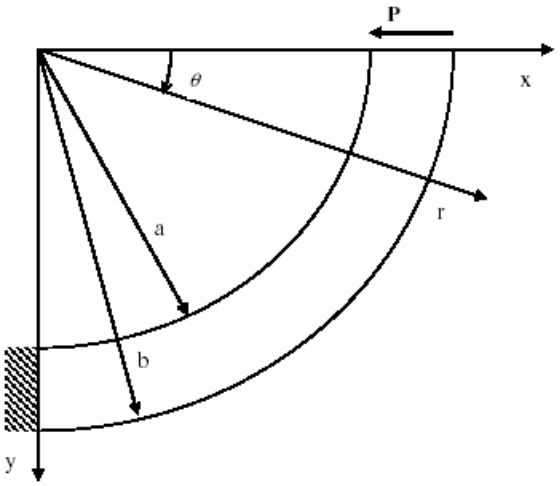

Figure 11 : A curved beam under a end load

with the constants are given as

$$
\begin{aligned}
N &= a^2 - b^2 + \left(a^2 + b^2\right) \log \frac{b}{a} \\
A &= \frac{1}{2N} \; B = -\frac{a^2 b^2}{2N} \\
D &= -\frac{a^2 + b^2}{2N} \; L = D\pi \\
K &= -\left(D(1-\nu) \log r_0 + A(1-3\nu) r_0^2 + \frac{B(1+\nu)}{r_0^2} \right) \\
r_0 &= \frac{a+b}{2}
\end{aligned}
\tag{33}
$$

The problem is solved for the plane stress condition, with $P = 1$, $E = 1$, $a = 13$, $b = 17$, and $\nu = 0.25$. Regular uniform nodal configurations with nodal distance, d, of 2.0, 1.0, 0.5 and 0.33 are used. The corresponding numbers of the nodes are 39, 125, 441, and 949. The nodal configuration of $d = 1.0$ is shown in Fig. 12.

For the curved beam, the displacement and stress fields are more complicated than those in a straight beam, with many non-polynomial terms. However, the simulation using the MLS with the first order monomial basis is still accurate. The horizontal and vertical displacements for the nodal configuration with $d = 0.5$ are shown in Fig. 13 and good agreement with the analytical solutions is obtained.

Here and in the following parts for the curved beam problem, the relative displacement error is defined through

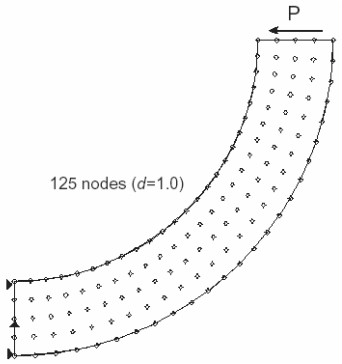

Figure 12 : The nodal configuration of the curved beam for d=1.0

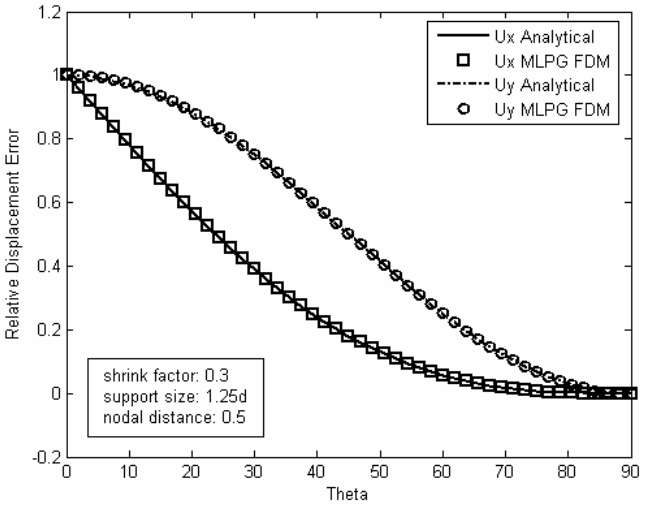

Figure 13 : The normalized vertical and horizontal displacement of the curved beam under the end load

the relative error of the maximum vertical and horizontal displacement as

$$
\varepsilon = \sqrt{\frac{1}{2}\left[\left(\frac{\vec{u}_x - u_x}{u_x} \right)^2 + \left(\frac{\vec{u}_y - u_y}{u_y} \right)^2 \right]} \tag{34}
$$

Here, u_x and u_y are the analytical displacement components at the center of the beam end; while $\vec{u}_x$ and $\vec{u}_y$ are the corresponding displacement components obtained by the MLPG mixed finite difference simulations. Fig. 14 and Fig. 15 show the influence of the shrink factor and the support size, respectively. Similar to the results in the cantilever beam, a moderate shrink factor and small support size lead to better results for the current beam

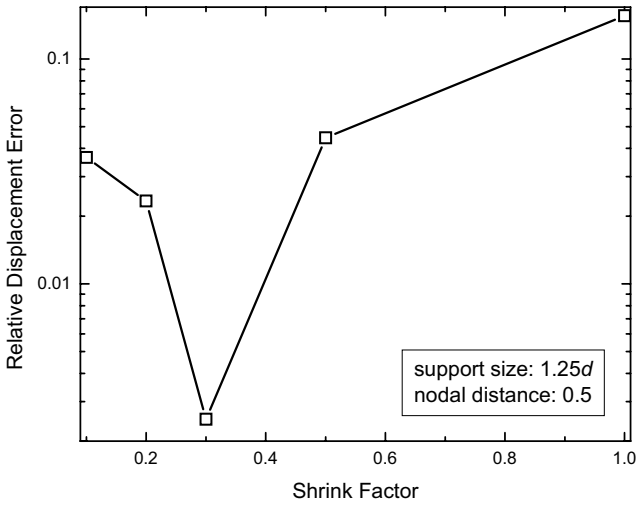

Figure 14 : The influence of the shrink factor in the curved beam under the end load

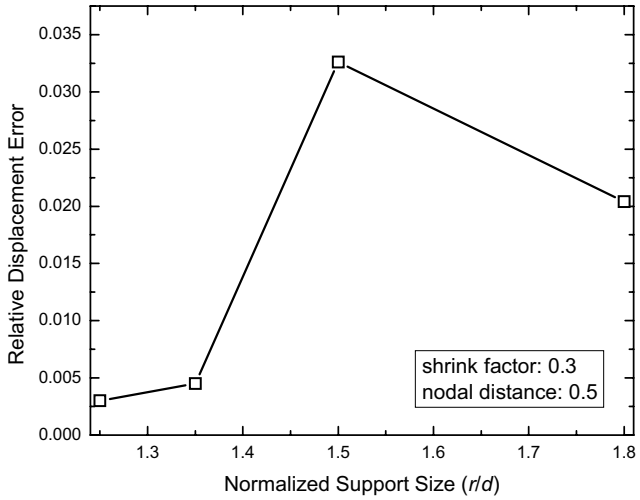

Figure 15 : The influence of the support size in the curved beam under the end load

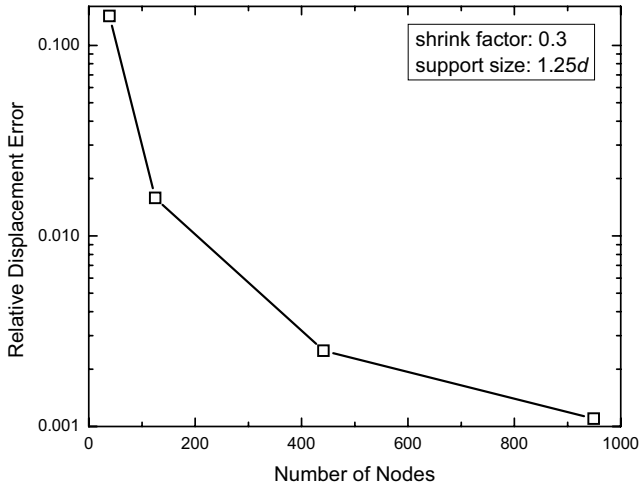

Figure 16 : The convergence rate of the curved beam under the end load

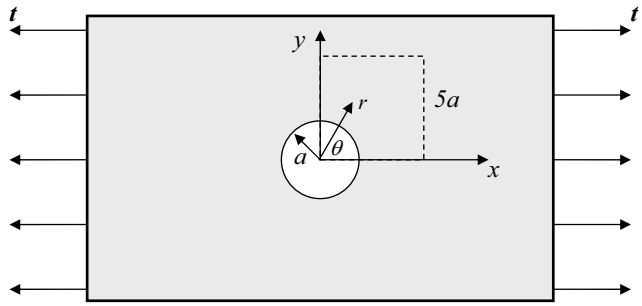

Figure 17 : An infinite plate with a circular hole under a uniaxial load

problems. Fig. 16 shows the stable convergence rate for the curved beam.

4.4 Infinite Plate with a Circular Hole

Finally, we show the computational results of an infinite plate with a circular hole subjected to a uniaxial traction P at infinity as shown in Fig. 17. The exact solutions for stresses and displacements for this problem are

$$\begin{aligned}
\sigma_x &= P\left\{1-\frac{a^2}{r^2}\left[\frac{3}{2}\cos(2\theta)+\cos(4\theta)\right]+\frac{3a^4}{2r^4}\cos(4\theta)\right\}\\
\sigma_y &= -P\left\{\frac{a^2}{r^2}\left[\frac{1}{2}\cos(2\theta)-\cos(4\theta)\right]+\frac{3a^4}{2r^4}\cos(4\theta)\right\}\\
\sigma_{xy} &= -P\left\{\frac{a^2}{r^2}\left[\frac{1}{2}\sin(2\theta)+\sin(4\theta)\right]-\frac{3a^4}{2r^4}\sin(4\theta)\right\}
\end{aligned} \tag{35}$$

and

$$u_r = \frac{P}{4G}\left\{ r\left[\frac{\kappa-1}{2}+\cos(2\theta)\right] + \frac{a^2}{r}\left[1+(1+\kappa)\cos(2\theta)\right] - \frac{a^4}{r^3}\cos(2\theta)\right\}$$
$$u_\theta = \frac{P}{4G}\left\{(1-\kappa)\frac{a^2}{r} - r - \frac{a^4}{r^3}\right\}\sin(2\theta) \quad (36)$$

respectively. In the above equations, G is the shear modulus and $\kappa = (3-\nu)/(1+\nu)$ with ν the Poisson's ratio. Due to symmetry, only the upper right square quadrant of the plate is modeled [see Fig. 17]. The edge length of the square is $5a$ with a being the radius of the circular hole. Symmetry boundary conditions are imposed on the left and bottom edges, and the tractions obtained from the analytical solution [Eq. (35)] are applied to the top and right edges.

The problem is solved using the MLPG mixed finite difference method, under a plane stress condition, with the following constants: $P = 1$, $E = 1$, and $\nu = 0.25$. Two regular nodal configurations with 126 and 380 nodes, and one irregular nodal configuration with 204 nodes are used in the current simulation. Fig. 18 shows the nodal configurations and the boundary conditions imposed on the edges. The MLS with linear basis is used in the simulation and the shrink factor is 0.3 and the support size is $1.25d$ with d being the average nodal distance. The horizontal displacement u_x along the bottom edge ($y = 0$) and the stress component σ_x along the left edge ($x = 0$) are shown in Fig. 19 and Fig. 20, respectively. Compared with the analytical solutions, good agreements are obtained for both the displacement and stress.

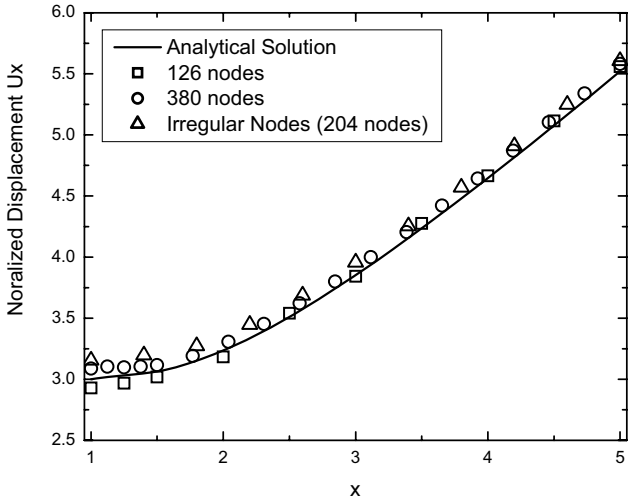

Figure 19 : The horizontal displacement along $y = 0$ for the two nodal configurations

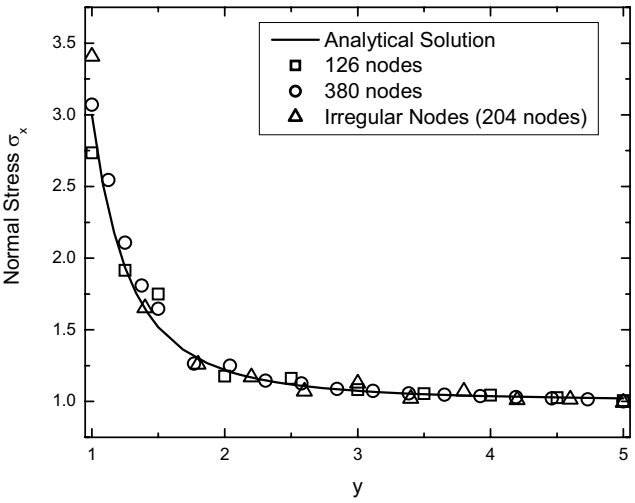

Figure 20 : The normal stress σ_x along $x = 0$ for the two nodal configurations

5 Closure

An MLPG mixed finite difference method is developed in this paper, in which the stresses and displacements are interpolated using the same shape functions independently. The generalized finite difference method (FDM) is developed to compute the derivatives of stresses, using the nodal values in the local domain (the neighbor nodes) of definition. To establish the system of equations, the linear force balance laws are enforced at both the in-domain as well as the boundary nodes through the same generalized FDM. The FDM is applied only to the nodal pairs of the neighbor nodes in the meshless interpolation, and it is suitable for solving the problems with the completed geometries. The stress components are computed from the traction boundary conditions through a local coordinate system, and the boundary stress values are imposed into the stress equations directly. Numerical examples show the suitability of the MLPG mixed finite difference method in solving various elasticity problems, including the ones with complex displacement and stress solutions.

Acknowledgement: This work is supported by the US Army.

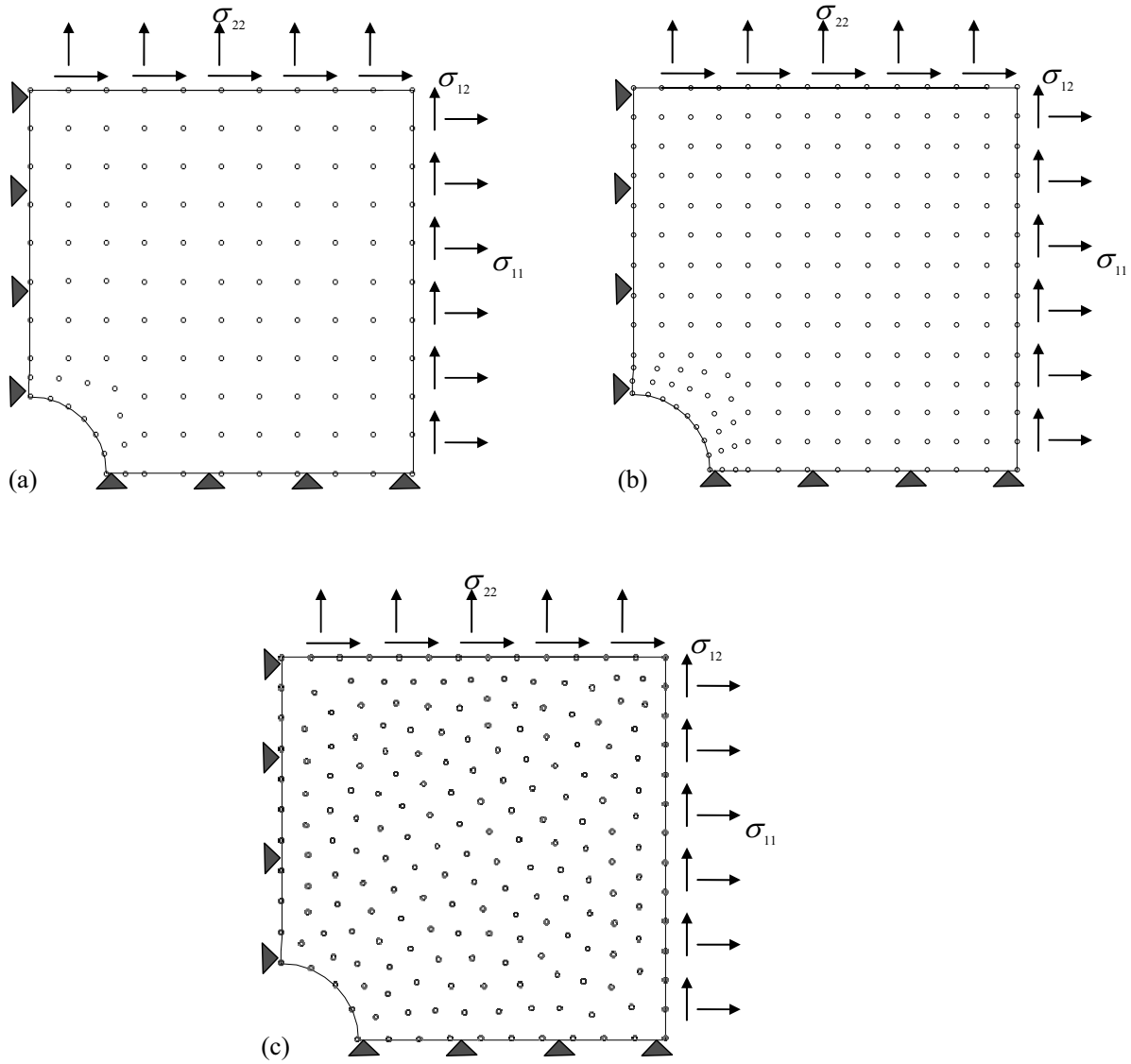

Figure 18 : The nodal configuration of the infinite plate with a circular hole (a) 126 nodes, (b) 380 nodes, and (c) 204 nodes with irregular arrangement

Reference

Atluri, S.N. (2004): The Meshless Local Petrov-Galerkin (MLPG) Method for Domain & Boundary Discretizations, Tech Science Press, 665 pages.

Atluri, S. N.; Han, Z. D.; Rajendran, A. M. (2004): A New Implementation of the Meshless Finite Volume Method, Through the MLPG "Mixed" Approach, *CMES: Computer Modeling in Engineering & Sciences*, vol. 6, no. 6, pp. 491-514.

Atluri, S. N.; Kim, H.G.; Cho, J.Y. (1999): A critical Assessment of the truly meshless local Petrov-Galerkin (MLPG) and local boundary integration equation (LBIE) methods, *Computational Mechanics*, Vol. 24, pp. 348-372.

Atluri, S. N.; Zhu, T. (1998): A new meshless local Petrov-Galerkin (MLPG) approach in computational mechanics. *Computational Mechanics*, Vol. 22, pp. 117-127.

Han. Z. D.; Atluri, S. N. (2004a): Meshless Local Petrov-Galerkin (MLPG) approaches for solving 3D Problems in elasto-statics, *CMES: Computer Modeling in Engineering & Sciences*, vol. 6 no. 2, pp. 169-188.

Han. Z. D.; Atluri, S. N. (2004b): A Meshless Local Petrov-Galerkin (MLPG) approaches for solving 3-dimensional elasto-dynamics, *CMC: Computers, Materials & Continua*, vol. 1 no. 2, pp. 129-140.

Han Z. D.; Liu H. T.; Rajendran, A. M; Atluri, S. N. (2006): The Applications of Meshless Local Petrov-Galerkin (MLPG) Approaches in High-Speed Impact, Penetration and Perforation Problems, *CMES: Computer Modeling in Engineering & Sciences*, in press.

Han Z. D.; Rajendran, A. M; Atluri, S. N. (2005): Meshless Local Petrov-Galerkin (MLPG) Approaches for Solving Nonlinear Problems with Large Deformation and Rotation, *CMES: Computer Modeling in Engineering & Sciences*, vol. 10, no. 1, pp. 12.

Jensen, P. S.; (1972): Finite difference techniques for variable grids, *Computers and Structures*, Vol.2:17-29.

Liu H. T.; Han Z. D.; Rajendran, A. M; Atluri, S. N. (2006a): Computational Modeling of Impact Response with the RG Damage Model and the Meshless Local Petrov-Galerkin (MLPG) Approaches, *CMC: Computers, Materials, & Continua*, in process.

Liu, H. T.; Han, Z. D.; Atluri, S. N. (2006b): Meshless Local Petrov-Galerkin (MLPG) Mixed Collocation Method for Elasticity Problems, *CMES: Computer Modeling in Engineering & Sciences*, In press.

Liszka, T. J.; Duarte, C. A. M.; Tworzydlo, W. W. (1996): hp-Meshless cloud method, *Computer Methods in Applied Mechanics and Engineering*, Vol 139, 263-288.

Perrone,N.; Kao, R. (1975): A general finite difference method for arbitrary meshes., *Computers and Structures*, Vol.5:45-58.

Timoshenko, S.P.; Goodier, J.N. (1970): Theory of Elasticity, 3^{rd} edition, McGraw Hill.